

Cite this: *J. Mater. Chem. C*,  
2024, 12, 18291

## A high-performance WS<sub>2</sub>/ZnO QD heterojunction photodetector with charge and energy transfer†

Yanjie Zheng,<sup>a</sup> Zhe Xu,<sup>b</sup> Kaixi Shi,<sup>b</sup> Jinhua Li,<sup>\*a</sup> Xuan Fang,<sup>c</sup> Zhenfeng Jiang<sup>a</sup>  
and Xueying Chu<sup>a</sup>

Two-dimensional/zero-dimensional (2D/0D) van der Waals heterojunctions have become a research hotspot for novel optoelectronic devices by virtue of their high light absorption and fast transportation. In previous studies, researchers preferred to construct heterojunctions with more matched energy bands to obtain high-performance photodetectors with efficient charge transfer. However, due to the limited configuration of 2D/0D heterojunctions, the coexistence mechanism of charge transfer and energy transfer has rarely been reported. In this work, we proposed a method to deliberately manipulate the defect states of ZnO quantum dots (QDs), which can achieve type-II band alignment and dipole-dipole interactions in the demonstrated WS<sub>2</sub>/ZnO heterojunction system. The coexistence of mechanisms is confirmed by photoluminescence (PL) and time-resolved photoluminescence (TRPL). As a result, the photodetector exhibits a high-responsivity (*R*) of 1120 A W<sup>-1</sup> and a high-detectivity (*D*\*) of 3.23 × 10<sup>12</sup> Jones. Moreover, the device reaches an ultra-fast response speed of 15 ns, which is one of the fastest response speeds of the current 2D/0D heterojunction photodetectors. The high photoresponse is attributed to the efficient interfacial carrier dynamics. Our work provides a new avenue for the coexistence of multiple mechanisms in 2D/0D heterojunctions, which is beneficial for the development of high-performance optoelectronic devices.

Received 27th August 2024,  
Accepted 7th October 2024

DOI: 10.1039/d4tc03659j

rsc.li/materials-c

### Introduction

2D/0D heterojunctions are widely applied in the fields of electronics and optoelectronics.<sup>1–15</sup> 2D materials generally exhibit high electron mobility. For example, WS<sub>2</sub> has a room-temperature electron mobility of 320 cm<sup>2</sup> V<sup>-1</sup> s<sup>-1</sup>, which enables rapid electron transfer.<sup>16</sup> 0D QDs, as an efficient light absorbing material, can compensate for the lack of light absorption in 2D materials. For example, ZnO QDs,<sup>17,18</sup> SnO<sub>2</sub> QDs,<sup>19</sup> PbS QDs,<sup>20,21</sup> etc. were reported to enhance the light absorption of 2D materials and broaden the spectral response range. However, the limited contact (point-to-face) of 2D/0D

heterojunctions is unfavorable for the separation of photogenerated electron-hole pairs and leads to a limited response speed of the heterojunction photodetector.<sup>22</sup>

Interfacial carrier dynamics in 2D/0D heterojunctions are inextricably linked to the photoelectric conversion efficiency of photodetectors. Charge transfer and energy transfer are important components of interfacial carrier dynamics.<sup>23</sup> In recent years, researchers have used energy band engineering and interfacial engineering to improve charge transfer efficiency, thereby enhancing the performance of photodetectors. For example, researchers focus on using materials with diverse bandgaps to construct types-II band alignment that enhance the separation efficiency of photogenerated electron-hole pairs.<sup>24–29</sup> Researchers have also proposed achieving interfacial passivation by processing defects and dangling bonds on the surface of transition-metal dichalcogenides (TMDCs), which suppresses the capture of carriers by defects.<sup>30–34</sup> Förster energy transfer, as a primarily reported non-radiative energy transfer, affects the performance of heterojunction photodetectors through dipole-dipole interactions between materials.<sup>23</sup> For example, Lai *et al.* selected matching QDs and 2D materials to construct a 2D-MoS<sub>2</sub>/0D-CdSe@ZnS QD heterojunction.<sup>35</sup> Attributed to non-radiative energy transfer between MoS<sub>2</sub> and QDs, the responsivity of the photodetector is increased by 14 times. Can we only use one method to achieve the combined

<sup>a</sup> Nanophotonics and Biophotonics Key Laboratory of Jilin Province, School of Physics, Changchun University of Science and Technology, Changchun, Jilin 130022, People's Republic of China. E-mail: shikaixi@cust.edu.cn, lijh@cust.edu.cn

<sup>b</sup> Changchun High-tech Industrial Development Zone, Shangde Academy of Jilin University, Changchun, Jilin 130000, People's Republic of China

<sup>c</sup> State Key Laboratory of High Power Semiconductor Laser, School of Science, Changchun University of Science and Technology, Changchun, Jilin 130022, People's Republic of China

† Electronic supplementary information (ESI) available: Fig. S1: the preparation process and optical characterization of ZnO QDs. Fig. S2: the UV photoresponse of the WS<sub>2</sub> and WS<sub>2</sub>/ZnO QD devices under 325 nm laser irradiation. Fig. S3: the energy band diagram of the WS<sub>2</sub>/Al<sub>2</sub>O<sub>3</sub>/ZnO QDs device. See DOI: <https://doi.org/10.1039/d4tc03659j>

effect of charge transfer and non-radiative energy transfer to improve the performance of the devices? Inspired by the above work, we deliberately designed a method to manipulate the defect states of ZnO QDs in order to achieve type-II band alignment and dipole-dipole interactions of WS<sub>2</sub> and ZnO QDs. This allows for the coexistence of charge transfer and non-radiative energy transfer. As a result, the improved performance of the heterojunction photodetector can be attributed to two reasons: (I) by introducing oxygen interstitials, the Fermi energy level of the ZnO QDs is close to the valence band, which widens the Fermi level gap between the two materials. The type-II band alignment results in a strong built-in electric field at the interface, which improves the separation efficiency of photo-generated electron-hole pairs. (II) By introducing defect states, the ZnO QDs broaden their luminescence range from the ultraviolet (UV) region to the visible region, which matches the absorption of WS<sub>2</sub>. This provides a platform for dipole-dipole interactions between two materials.

## Result and discussion

Fig. 1a shows a schematic of the WS<sub>2</sub>/ZnO QDs heterojunction photodetector. The photodetector was successfully prepared by mechanically stripping the WS<sub>2</sub> bulk material onto the fork-finger electrodes, followed by spin-coating the optimized ZnO QDs. By modulating the molar ratio of OH<sup>-</sup>: Zn<sup>2+</sup>, the prepared ZnO QDs produce oxygen interstitials. This forms the basis for the coexistence of multiple mechanisms in the WS<sub>2</sub>/ZnO QDs heterojunction. The synthesis steps are shown in Fig. S1a (ESI<sup>†</sup>). In addition, by modulating the concentration of ZnO QDs, the aggregation of QDs was suppressed, and strong luminescence was achieved (Fig. S1b–d, ESI<sup>†</sup>). Strong luminescence will generate a larger spectral overlap with the absorption of WS<sub>2</sub>, which facilitates dipole-dipole interactions and creates conditions for non-radiative energy transfer. Transmission electron microscopy (TEM) analysis demonstrated the good dispersibility of ZnO QDs (Fig. 1b). The inset shows the size distribution of the ZnO QDs with an average size of  $\sim 7.4 (\pm 0.5)$  nm. Fig. 1c shows the morphology of the WS<sub>2</sub>/ZnO QDs heterojunction photodetector observed by scanning electron microscopy (SEM), where WS<sub>2</sub> is used as the channel material on the Au fork finger electrode. The chemical composition of the heterojunction photodetector was determined by energy dispersive X-ray spectroscopy (EDS). The detected spectra from EDS confirm the presence of Zn, W and S elements in the heterojunction (Fig. 1d–f). Afterwards we performed Raman characterization of the heterojunction. Fig. 1g shows the Raman peaks of WS<sub>2</sub> under 532 nm laser excitation. The peak at  $356.5 \text{ cm}^{-1}$  corresponds to the in-plane vibration mode  $E_{2g}^1$ . The peak at  $418.3 \text{ cm}^{-1}$  is designated as the out-of-plane vibration mode  $A_{1g}$  for the S atoms. The frequency difference ( $\Delta\omega$ ) between the  $E_{2g}^1$  and  $A_{1g}$  modes is about  $61.8 \text{ cm}^{-1}$ , confirming the monolayer structure.<sup>36,37</sup> The peak at  $350.5 \text{ cm}^{-1}$  corresponds to the longitudinal acoustic mode 2LA(M). Fig. 1h shows the Raman peaks of ZnO QDs under 325 nm laser excitation. The peak at  $574 \text{ cm}^{-1}$  corresponds to the  $A_1$  (LO) phonon mode, and the other peaks are

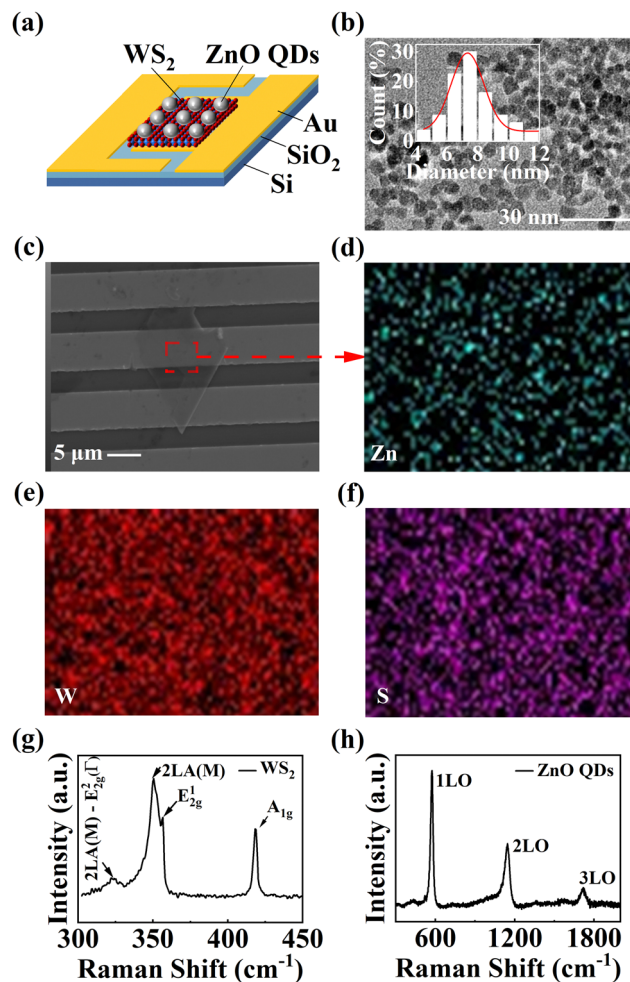


Fig. 1 Characterization of the WS<sub>2</sub>/ZnO QD heterojunction photodetector. (a) Schematic diagram of the WS<sub>2</sub>/ZnO QD heterojunction photodetector. (b) TEM image of the ZnO QDs and the size distribution of the ZnO QDs (inset). (c) SEM image of the WS<sub>2</sub>/ZnO QDs heterojunction photodetector. The SEM-EDS element mapping of the Zn (d), W (e), and S (f) from the WS<sub>2</sub>/ZnO QD heterojunction. (g) Raman spectrum of the WS<sub>2</sub> under 532 nm laser excitation. (h) Raman spectrum of the ZnO QDs under 325 nm laser excitation.

higher-order peaks of LO phonons.<sup>38</sup> SEM, EDS and Raman together demonstrated that the heterojunction was successfully constructed.

To evaluate the effect of ZnO QDs for the WS<sub>2</sub> device, we compared the optoelectronic properties of WS<sub>2</sub>, pristine WS<sub>2</sub>/ZnO and annealed WS<sub>2</sub>/ZnO devices. Due to the surface defect states generated during the preparation of ZnO QDs, such as surface zinc vacancies, annealing is used to reduce the impact of surface defect states on charge transfer. Meanwhile, oxygen interstitials become the main defect of annealed ZnO QDs, which improves the non-radiative energy transfer efficiency between ZnO QDs and WS<sub>2</sub>. We used the photoresponse test system (see Fig. 2a) to test the devices, which includes a Keithley 2400, probe station and 532 nm laser. Fig. 2b–d show the photoresponse characteristics for WS<sub>2</sub>, pristine WS<sub>2</sub>/ZnO and annealed WS<sub>2</sub>/ZnO devices (at zero gate voltage). Compared to

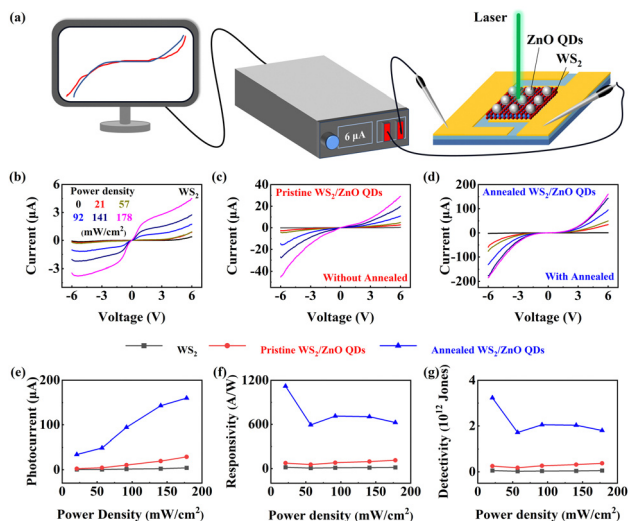


Fig. 2 (a) Schematic diagram of the photoresponse test system. The  $I$ - $V$  curves of  $\text{WS}_2$  (b), pristine  $\text{WS}_2/\text{ZnO}$  QD (c), and annealed  $\text{WS}_2/\text{ZnO}$  QD (d) photodetectors under laser irradiation with different optical power densities. The dependence of photocurrent (e), responsivity (f) and detectivity (g) on different optical power densities for  $\text{WS}_2$ , pristine  $\text{WS}_2/\text{ZnO}$  QD, and annealed  $\text{WS}_2/\text{ZnO}$  QD photodetectors (at a 6 V bias).

the  $\text{WS}_2$  device, the source-drain current values are enhanced for the construction of 2D/0D heterojunction devices. In order to quantitatively analyze the effect of ZnO QDs on the performance of the  $\text{WS}_2$  photodetector, we calculated and compared the photocurrent ( $I_{\text{ph}}$ ), responsivity ( $R$ ) and detectivity ( $D^*$ ) of the devices. The  $I_{\text{ph}}$  and  $R$  reflect the detection capability of the photodetector.<sup>39,40</sup> The  $D^*$  is an indicator of the photodetector to detect weak light signals.<sup>41</sup> The  $I_{\text{ph}}$ , the  $R$  and the  $D^*$  can be calculated using the following equations:

$$I_{\text{ph}} = I_{\text{light}} - I_{\text{dark}}$$

$$R = \frac{I_{\text{ph}}}{P_{\text{opt}} \times A}$$

$$D^* = \frac{A^{1/2} R}{(2qI_{\text{dark}})^{1/2}}$$

where  $I_{\text{ph}}$  is the photocurrent,  $I_{\text{light}}$  is the current value under laser irradiation,  $I_{\text{dark}}$  is the current value without laser irradiation,  $P_{\text{opt}}$  is the optical power density,  $A$  is the effective light absorption area of the device, and  $q$  is the unit charge. Fig. 2e shows the relationship between photocurrent and optical power density, where the photocurrent increases with increasing optical power density. At the optical power density of  $178 \text{ mW cm}^{-2}$ , the annealed  $\text{WS}_2/\text{ZnO}$  QD device achieves a maximum photocurrent of  $\sim 159 \mu\text{A}$ , which is a 39 times improvement over the  $\text{WS}_2$  device. Fig. 2f and g show comparative data for the  $R$  and  $D^*$  of photodetectors. As the optical power density increases, a decrease in  $R$  and  $D^*$  was observed, which is attributed to carrier scattering and increased recombination under laser irradiation.<sup>42</sup> At an optical power density of  $21 \text{ mW cm}^{-2}$ , the  $R$  and  $D^*$  of the annealed  $\text{WS}_2/\text{ZnO}$  QD

device were improved to 68 and 57 times compared to that of the  $\text{WS}_2$  device, respectively. The highest  $R$  is up to  $\sim 1120 \text{ A W}^{-1}$  and the  $D^*$  is up to  $\sim 3.23 \times 10^{12}$  Jones. In addition, to demonstrate the broad spectral response of the devices, the UV photoresponse of the devices was tested. Fig. S2 (ESI<sup>†</sup>) provides a more detailed description. In this work, the annealed  $\text{WS}_2/\text{ZnO}$  QD device exhibited the best performance, which is attributed to the fact that annealing can reduce the number of surface defect states in ZnO QDs and improve the interface contact quality. This results in faster separation and transportation of photo-generated carriers for the  $\text{WS}_2/\text{ZnO}$  QDs heterojunction device. In order to reveal the improvement of device performance, the interface carrier dynamics from  $\text{WS}_2$  and ZnO QDs are analyzed in detail later.

Response speed is a significant parameter for evaluating the performance of photodetectors. Fig. 3a shows a schematic of the response speed test system. To evaluate the optical storage capability of the annealed  $\text{WS}_2/\text{ZnO}$  QD device, it was tested under laser irradiation with different power densities. Fig. 3b shows the photoswitching characteristics of the annealed  $\text{WS}_2/\text{ZnO}$  QDs device. As the optical power density increases, the switching ratio is improved. The maximum current values for 300 cycles under laser irradiation with different optical power densities are shown in Fig. 3c, which demonstrates the good

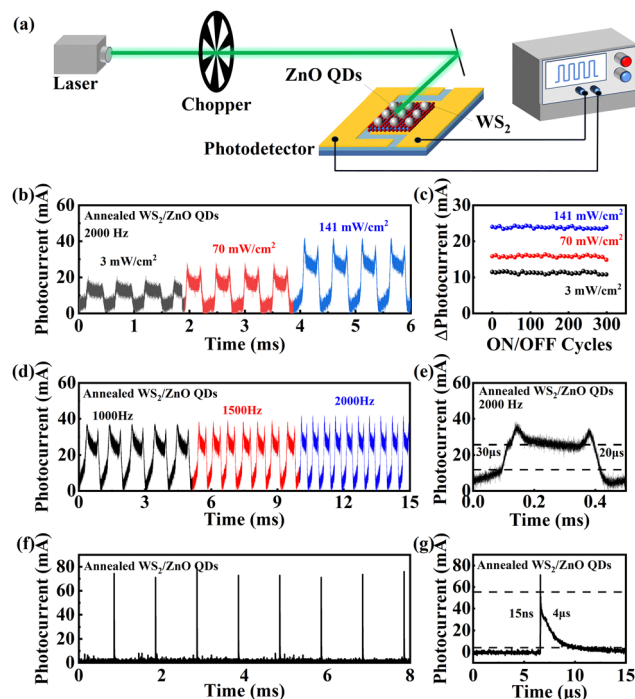


Fig. 3 Evaluation of the photoresponse speed and stability of the annealed  $\text{WS}_2/\text{ZnO}$  QD device. (a) Schematic of the response speed test system. Impulse response (b) and stability (c) of the device under laser irradiation with different optical power densities. (d) Impulse response of the device under laser irradiation with different frequencies. (e) One photoresponse cycle for the device. Impulse response (f) and one femtosecond-pulsed photoresponse cycle (g) of the device under a femtosecond-pulsed laser with a pulse-frequency of 1 kHz and a pulse-width of 50 fs.

stability of the device. The stable photoresponse under different light excitations leads to optical storage applications.<sup>43</sup> In order to evaluate the response speed of the device, the device was tested at different frequencies of the chopper. Fig. 3d shows the photoswitching properties of the annealed WS<sub>2</sub>/ZnO QD device at 1000, 1500 and 2000 Hz. As the chopper frequency increased from 1000 Hz to 2000 Hz, the device still maintains a stable photoresponse output. When the frequency of the chopper is 2000 Hz, the device can achieve a rise time of  $\sim 30 \mu\text{s}$  and a decay time of  $\sim 20 \mu\text{s}$  (see Fig. 3e). Due to the speed limitation of the chopper, the response speed of the device is limited to  $\mu\text{s}$ . To evaluate the ultimate response speed of the annealed WS<sub>2</sub>/ZnO QD device, we used a femtosecond-pulse laser for testing. Fig. 3f shows the photoswitching properties of the annealed WS<sub>2</sub>/ZnO QDs device under femtosecond-pulsed laser excitation. The device accurately responds to each pulse signal and exhibits an ultra-fast response speed with a rise time of  $\sim 15 \text{ ns}$  and a decay time of  $\sim 4 \mu\text{s}$  (Fig. 3g). Compared with the 2D/0D heterojunction photodetectors based on TMDCs reported in previous literature, the WS<sub>2</sub>/ZnO QD heterojunction photodetector exhibits one of the fastest response speeds (Table 1). The ultra-fast response speed of the device is attributed to the combination of charge transfer and non-radiative energy transfer, which improves the efficiency of carrier separation and transportation.

We proposed a method for regulating ZnO QD defect states, which can be applied to coexistence mechanisms of heterojunctions. However, in addition to oxygen interstitials, surface defect states are inevitably generated, which can capture carriers. Therefore, annealing is adopted to reduce the impact of surface defect states. Next, we will evaluate the promoting effect of annealing on the 2D/0D heterojunction. Fig. 4a shows the Raman spectra of three devices, where the E<sub>2g</sub><sup>1</sup> peak and the A<sub>1g</sub> peak correspond to in-plane and out-of-plane vibration modes, respectively. The A<sub>1g</sub> peak of WS<sub>2</sub> is sensitive to electron transfer, while the E<sub>2g</sub><sup>1</sup> peak is not sensitive to electron transfer.<sup>16,53</sup> As shown in Fig. 4b, the A<sub>1g</sub> peak of the pristine WS<sub>2</sub>/ZnO exhibits a blueshift compared to the A<sub>1g</sub> peak of WS<sub>2</sub>. We inferred that this is related to the decrease in electron concentration of WS<sub>2</sub>. Compared with the pristine WS<sub>2</sub>/ZnO, the A<sub>1g</sub> peak of annealed WS<sub>2</sub>/ZnO exhibits a further blueshift.

This proves that annealing facilitates electron transfer. Fig. 4c shows the band diagrams of WS<sub>2</sub> and ZnO QDs before contact. The Fermi level of WS<sub>2</sub> is higher than that of ZnO QDs, and electrons will flow from WS<sub>2</sub> to ZnO QDs. The further blueshift of the A<sub>1g</sub> peak was attributed to annealing enhancing the built-in electric field, which further reduced the electron concentration in WS<sub>2</sub>. That is, the shift of the A<sub>1g</sub> peak can reflect the electron transfer efficiency in the heterojunction. As a result, annealing has two effects in the WS<sub>2</sub>/ZnO QDs heterojunction: (I) annealing improves the strength of the built-in electric field, thus promoting charge transfer in the heterojunction. (II) Annealing enhances the interface contact quality and suppresses the surface defect states of ZnO QDs, thereby reducing the capture of carriers by defects. Therefore, annealing is beneficial for heterojunctions with type-II band alignment. To confirm charge transfer and the effect of annealing in the heterojunction, the PL spectra of three devices were further discussed.

Fig. 5a compares the PL spectra of the WS<sub>2</sub>, pristine WS<sub>2</sub>/ZnO and annealed WS<sub>2</sub>/ZnO. Obviously, after the formation of the heterojunction, PL quenching was observed. Compared to the pristine WS<sub>2</sub>/ZnO heterojunction, the annealed WS<sub>2</sub>/ZnO heterojunction exhibits stronger PL quenching from 48% to 74%. To analyze this variation, PL spectra were deconvoluted into two sub-peaks, one from the charged ions (X<sup>-</sup>) and the other from the neutral excitons (X<sup>0</sup>), as displayed in Fig. 5b. The areas of X<sup>-</sup> and X<sup>0</sup> represent the concentrations of charged ions and neutral excitons in WS<sub>2</sub>, respectively. Next, we discussed in depth the area ratio (Fig. 5c) and peak shift (Fig. 5d) of X<sup>-</sup> and X<sup>0</sup> for charge transfer. After the formation of the heterojunction, it is observed that the area ratio of X<sup>-</sup> increases and the area ratio of X<sup>0</sup> decreases. This indicates that the electrons in the ZnO QDs were transferred to the WS<sub>2</sub> under the 532 nm laser excitation. Meanwhile, it was confirmed that our proposed 2D/0D heterojunction system can achieve efficient interface carrier dynamics. After forming the heterojunction, the shift of X<sup>-</sup> and X<sup>0</sup> peaks was observed, which is attributed to charge transfer in the heterojunction. The concentration of X<sup>-</sup> is increased, and the energy of photons is enhanced through the recombination of electrons and holes, resulting in the shift of X<sup>-</sup>. The concentration of X<sup>0</sup> is reduced, which means that the distance between electrons and holes increases. The Coulomb

Table 1 Performance comparison of the reported 2D/0D heterojunction photodetectors

Device material	Coexistence	Responsivity (A W <sup>-1</sup> )	Detectivity (Jones)	Response speed ( $\mu\text{s}$ )	Lifetime (ns)	Ref.
SnSe <sub>2</sub> /SnO <sub>2</sub> QDs	No	$1.68 \times 10^{-2}$	$2.6 \times 10^9$	$5 \times 10^5$	—	19
MoS <sub>2</sub> /CdSe@ZnS QDs	No	$2.6 \times 10^{-2}$	—	$2.4 \times 10^5$	11.2	35
WS <sub>2</sub> /AIGS QDs	No	$3.3 \times 10^3$	$1.3 \times 10^{13}$	$3 \times 10^7$	54.26	44
MoS <sub>2</sub> /CdSe QDs	Yes	$5 \times 10^2$	—	$1.59 \times 10^5$	0.43	45
MoS <sub>2</sub> /CdSe@ZnS QDs	No	$4 \times 10^2$	—	$1.85 \times 10^5$	0.32	45
MoS <sub>2</sub> /CuInS <sub>2</sub> QDs	No	1.83	$7.05 \times 10^{11}$	$5.96 \times 10^6$	—	46
WSe <sub>2</sub> /CsPbBr <sub>3</sub> PQDs	No	$2.1 \times 10^2$	$9.1 \times 10^{12}$	$1.27 \times 10^6$	20	47
MoS <sub>2</sub> /SnS <sub>2</sub> QDs	No	$4.35 \times 10^2$	$7.19 \times 10^{12}$	$1 \times 10^5$	—	48
Bi <sub>2</sub> Se <sub>3</sub> /CsPbBr <sub>2</sub> I QDs	No	$1.44 \times 10$	$4.0 \times 10^{11}$	$8.2 \times 10$	3.6	49
WS <sub>2</sub> /WO <sub>3</sub> QDs	No	$2.51 \times 10^2$	$1.89 \times 10^{14}$	$6.4 \times 10^5$	0.3	50
WS <sub>2</sub> /CdSe QDs	No	$1.96 \times 10^{-5}$	$5.1 \times 10^4$	$5.7 \times 10$	2.6	51
MoS <sub>2</sub> /ZnCdSe@ZnS QDs	No	$3.7 \times 10^4$	$1 \times 10^{12}$	$3 \times 10^5$	—	52
<b>WS<sub>2</sub>/ZnO QDs</b>	<b>Yes</b>	<b><math>1.12 \times 10^3</math></b>	<b><math>3.23 \times 10^{12}</math></b>	<b><math>1.5 \times 10^{-3}</math></b>	<b>1.96</b>	<b>This work</b>

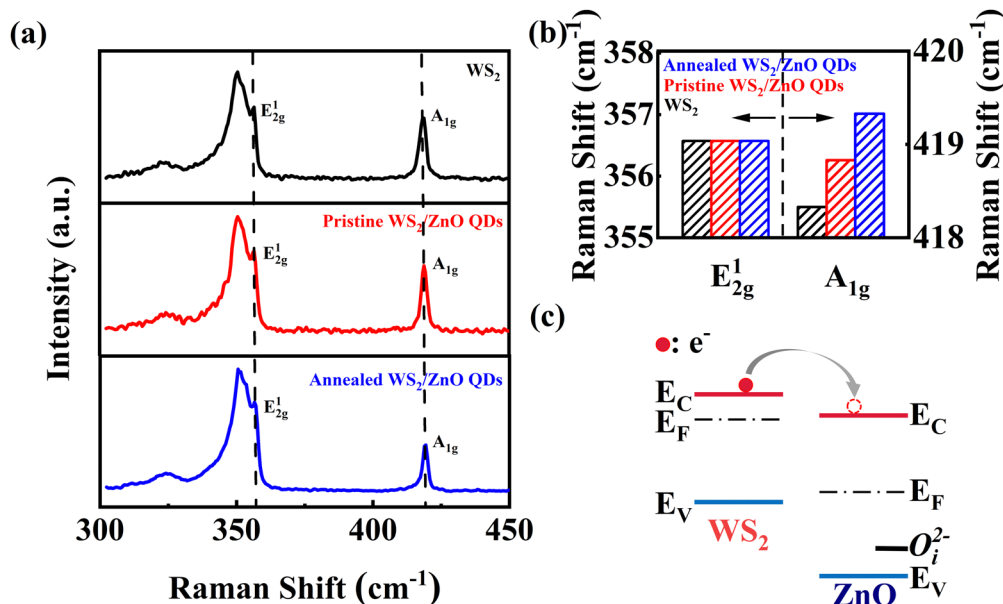


Fig. 4 (a) Raman spectra of  $\text{WS}_2$ , pristine  $\text{WS}_2/\text{ZnO}$  QDs and annealed  $\text{WS}_2/\text{ZnO}$  QDs under 532 nm laser excitation. (b) Statistical analysis of  $\text{E}_{2g}^1$  and  $\text{A}_{1g}$  Raman shifts for  $\text{WS}_2$ , pristine  $\text{WS}_2/\text{ZnO}$  QDs and annealed  $\text{WS}_2/\text{ZnO}$  QDs. (c) The band diagram of the Fermi levels for  $\text{WS}_2$  and  $\text{ZnO}$  QDs before alignment.

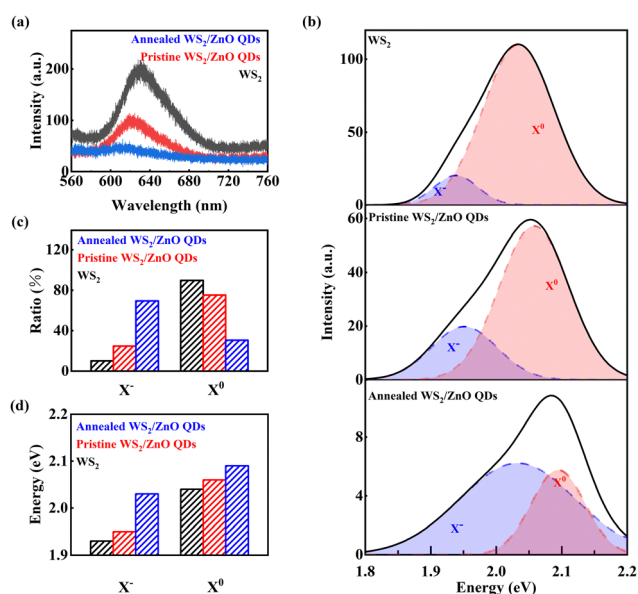


Fig. 5 (a) PL spectra of  $\text{WS}_2$ , pristine  $\text{WS}_2/\text{ZnO}$  QDs and annealed  $\text{WS}_2/\text{ZnO}$  QDs under 532 nm laser excitation. (b) The PL spectra of three devices were fitted as  $\text{X}^-$  and  $\text{X}^0$  by Gaussian deconvolution. The statistics included the area ratio (c) and the peak shift (d) of  $\text{X}^-$  and  $\text{X}^0$  for three devices.

interaction is enhanced by that. This will improve the binding energy of  $\text{X}^0$ , causing a blueshift in the  $\text{X}^0$  peak.<sup>54,55</sup> After annealing, the further increase in the  $\text{X}^-$  area and the further shift of the  $\text{X}^-$  peak once again demonstrate that annealing can optimize the 2D/0D heterojunction system.

In 2D/0D heterojunctions, the overlap between the PL spectrum and the absorption spectrum allows for non-radiative energy transfer.<sup>56,57</sup> Fig. 6a shows the schematic diagram of non-radiative energy transfer between  $\text{WS}_2$  and  $\text{ZnO}$  QDs,

where the photogenerated electron-hole pair moved from  $\text{ZnO}$  QDs to  $\text{WS}_2$  without emitting photons.<sup>58</sup> Fig. 6b shows the PL spectrum of  $\text{ZnO}$  QDs and the absorption spectrum of  $\text{WS}_2$ , and spectral overlap was observed. The PL spectrum of  $\text{ZnO}$  QDs was deconvoluted into four sub-peaks to show the effect of defects on the optical properties of  $\text{ZnO}$  QDs. The UV band emission centered at  $\sim 378$  nm corresponds to the near band edge (NBE) emission, which is the reason for the free exciton recombination of  $\text{ZnO}$ .<sup>59</sup> The peaks at  $\sim 405$  nm and  $\sim 428$  nm are attributed to surface zinc vacancies and their associated lattice defects, respectively.<sup>60,61</sup> Surface zinc vacancies and their associated lattice defects can capture carriers, which is unfavorable to charge transfer. So annealing is used to solve this problem. The peak related to  $\sim 450$  nm is attributed to the oxygen interstitials in  $\text{ZnO}$ .<sup>59,62,63</sup> The oxygen interstitials were intentionally introduced into  $\text{ZnO}$  QDs. Due to the complete overlap between the PL spectrum of oxygen interstitials and the absorption spectrum of  $\text{WS}_2$ , dipole-dipole interactions are promoted, which is conducive to the generation of non-radiative energy transfer.

To confirm non-radiative energy transfer in the 2D/0D system, TRPL measurements were conducted (Fig. 6c). We used a two-phase exponential decay function to analyze fluorescence lifetime. After forming a heterojunction, a significant decrease in fluorescence lifetime was observed. The  $\tau_1$  decreased from 0.56 ns to 0.12 ns, and the  $\tau_2$  decreased from 12.21 ns to 1.84 ns (Fig. 6d). We speculated that this is related to the combined effect of charge transfer and non-radiative energy transfer. To prevent charge transfer between  $\text{WS}_2$  and  $\text{ZnO}$  QDs, we introduced wide bandgap  $\text{Al}_2\text{O}_3$  in the  $\text{WS}_2/\text{ZnO}$  QD heterojunction (Fig. S3, ESI†). The  $\tau_1$  and the  $\tau_2$  of the  $\text{WS}_2/\text{Al}_2\text{O}_3/\text{ZnO}$  QDs heterojunction were 0.43 ns and 5.33 ns (Fig. 6d). A decrease in fluorescence lifetime was still observed. This proves that charge

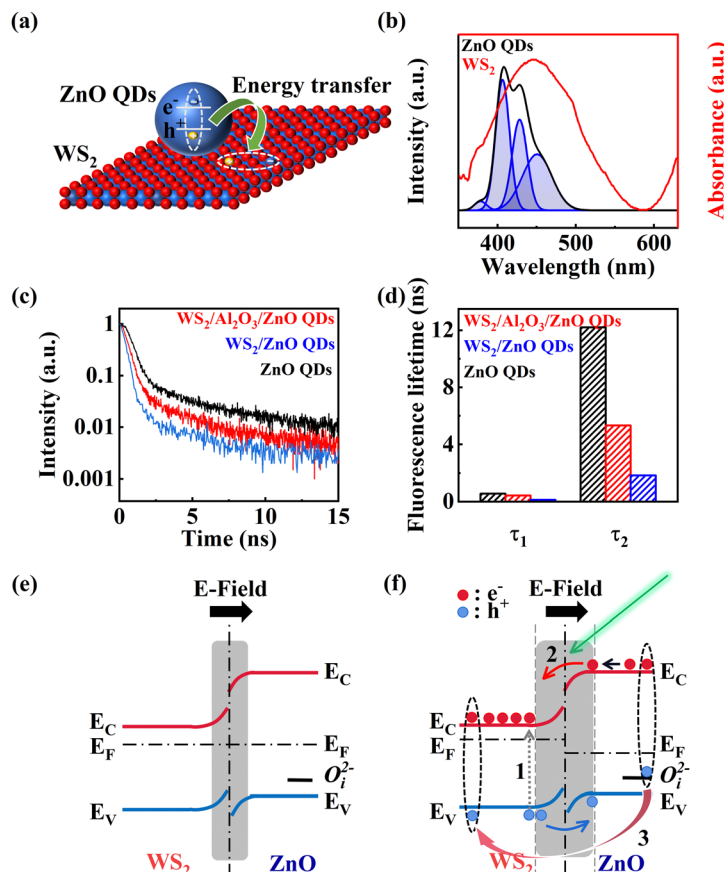


Fig. 6 (a) Energy transfer diagram of the  $\text{WS}_2/\text{ZnO}$  QDs heterojunction. (b) Spectra overlap between the  $\text{WS}_2$  absorption and the ZnO QD PL, and the PL spectrum was deconvoluted into four sub-peaks originating from UV emission ( $\sim 378$  nm) and blue emission ( $\sim 405$  nm,  $\sim 428$  nm and  $\sim 450$  nm). (c) Fluorescence lifetime traces of ZnO QDs,  $\text{WS}_2/\text{ZnO}$  QDs and  $\text{WS}_2/\text{Al}_2\text{O}_3/\text{ZnO}$  QDs under 375 nm laser excitation. (d) Statistics of  $\tau_1$  and  $\tau_2$  for ZnO QDs,  $\text{WS}_2/\text{ZnO}$  QDs and  $\text{WS}_2/\text{Al}_2\text{O}_3/\text{ZnO}$  QDs. Energy band diagram of the  $\text{WS}_2/\text{ZnO}$  QD heterojunction without laser irradiation (e) and with laser irradiation (f).

transfer and non-radiative energy transfer coexist in the  $\text{WS}_2/\text{ZnO}$  QDs heterojunction. Fig. 6e and f show the energy band diagrams of the  $\text{WS}_2/\text{ZnO}$  QD heterojunction before and after 532 nm laser irradiation. Due to the introduction of oxygen interstitials, the Fermi level of ZnO QDs is close to the valence band. The Fermi level difference between  $\text{WS}_2$  and ZnO QDs increases. A wide Fermi energy level difference is beneficial for the formation of type-II band arrangement in  $\text{WS}_2$  and ZnO QDs. When the heterojunction is irradiated with a 532 nm laser,  $\text{WS}_2$  generates photogenerated carriers (path 1), and the built-in electric field separates the photogenerated carriers (path 2). The electrons move towards  $\text{WS}_2$ , while the holes in  $\text{WS}_2$  move towards ZnO QDs. Non-radiative energy transfer works simultaneously to transfer excitons into  $\text{WS}_2$  (path 3), and the  $\text{WS}_2/\text{ZnO}$  QDs heterojunction achieves a combined effect of charge transfer and non-radiative energy transfer.

## Conclusions

In summary, a high-performance  $\text{WS}_2/\text{ZnO}$  QD heterojunction photodetector has been developed, which combines charge transfer and energy transfer by manipulating the defect states of ZnO QDs. The charge transfer in the heterojunction was

confirmed by the Raman blueshift and the increased concentration of  $\text{X}^-$  in the PL. The existence of non-radiative energy transfer in the heterojunction is substantiated by the quenching of fluorescence lifetime even after blocking charge transfer with  $\text{Al}_2\text{O}_3$ . As a result, the hybrid photodetector shows excellent performance with high responsivity ( $1120 \text{ A W}^{-1}$ ) and high detectivity ( $3.23 \times 10^{12}$  Jones), which are 71 times and 58 times higher than that of the  $\text{WS}_2$  device, respectively. Fortunately, the device's 15 ns response speed is one of the fastest reported 2D/0D heterojunction devices, attributed to the efficient interface carrier dynamics. The coexistence of multiple mechanisms in 2D/0D heterojunctions provides a new avenue for the development of high-performance low-dimensional photodetectors.

## Experimentation

### $\text{WS}_2$ base photodetector

At room temperature, a small amount of  $\text{WS}_2$  material was peeled off from the bulk material by 3 M tape, and the tape was repeatedly folded to obtain a single layer of  $\text{WS}_2$  by breaking van der Waals forces. Then, the tape was attached to the Au finger electrode and heated at  $60^\circ\text{C}$  for 20 minutes to enhance the adsorption between  $\text{WS}_2$  and the finger electrode. This

achieves a WS<sub>2</sub> based photodetector. The length of the Au forked electrode is 1400 μm and the width is 5 μm.

### ZnO QDs

1.4 g of potassium hydroxide (KOH) was dissolved in 60 ml of methanol (CH<sub>3</sub>OH). 2.96 g of zinc acetate dihydrate (Zn(CH<sub>3</sub>COO)<sub>2</sub>·2H<sub>2</sub>O) was dissolved in 120 ml of CH<sub>3</sub>OH. Two solutions were mixed and heated on a magnetic stirrer (temperature 60 °C) for 210 minutes before centrifugation. The bottom suspension was washed three times with methanol reagent. Finally, the obtained ZnO QDs were dispersed in a *n*-butanol solution.

### The WS<sub>2</sub>/ZnO QD photodetector

The obtained ZnO QD solution was uniformly dropped onto the WS<sub>2</sub> based photodetector and coated at 1000 rpm for 10 seconds, followed by another 20 seconds at 3000 rpm. The obtained photodetector was placed on an 80 °C heating plate and heated for 10 minutes.

## Author contributions

Yanjie Zheng: experiments, data curation, investigation, writing – original draft. Zhe Xu: data curation, formal analysis. Kaixi Shi and Jinhua Li: funding acquisition, project administration, resources, writing – review & editing, supervision. Xuan Fang: resources. Zhenfeng Jiang: data curation. Xueying Chu: supervision.

## Data availability

The data that support the findings of this study are available from the corresponding author upon reasonable request.

## Conflicts of interest

There are no conflicts to declare.

## Acknowledgements

The authors are immensely grateful to the National Natural Science Foundation of China (Grant No. 62174015), and the Department of Science and Technology of Jilin Province (Grant No. YDZJ202301ZYTS488).

## References

- V. Selamneni, S. K. Ganeshan and P. Sahatiya, All MoS<sub>2</sub> based 2D/0D localized unipolar heterojunctions as flexible broadband (UV-vis-NIR) photodetectors, *J. Mater. Chem. C*, 2020, **8**(33), 11593–11602.
- J. Fang, Z. Zhou and M. Xiao, *et al.*, Recent advances in low-dimensional semiconductor nanomaterials and their applications in high-performance photodetectors, *InfoMat*, 2020, **2**(2), 291–317.
- U. N. Noubé, C. Gréboval and C. Livache, *et al.*, Reconfigurable 2D/0D p–n Graphene/HgTe nanocrystal heterostructure for infrared detection, *ACS Nano*, 2020, **14**(4), 4567–4576.
- J. Shan, J. Li and X. Chu, *et al.*, Enhanced photoresponse characteristics of transistors using CVD-grown MoS<sub>2</sub>/WS<sub>2</sub> heterostructures, *Appl. Surf. Sci.*, 2018, **443**, 31–38.
- C. Zhao, D. Wang and J. Cao, *et al.*, Highly efficient 1D p-Te/2D n-Bi<sub>2</sub>Te<sub>3</sub> heterojunction self-driven broadband photodetector, *Nano Res.*, 2024, **17**(3), 1864–1874.
- L. Zeng, D. Wu and J. Jie, *et al.*, van der Waals epitaxial growth of mosaic-like 2D platinum ditelluride layers for room-temperature mid-infrared photodetection up to 10.6 μm, *Adv. Mater.*, 2020, **32**(52), 2004412.
- L. Zeng, W. Han and X. Ren, *et al.*, Uncooled mid-infrared sensing enabled by chip-integrated low-temperature-grown 2D PdTe<sub>2</sub> Dirac semimetal, *Nano Lett.*, 2023, **23**(17), 8241–8248.
- L. H. Zeng, D. Wu and S. H. Lin, *et al.*, Controlled synthesis of 2D palladium diselenide for sensitive photodetector applications, *Adv. Funct. Mater.*, 2019, **29**(1), 1806878.
- L. H. Zeng, S. H. Lin and Z. J. Li, *et al.*, Fast, self-driven, air-stable, and broadband photodetector based on vertically aligned PtSe<sub>2</sub>/GaAs heterojunction, *Adv. Funct. Mater.*, 2018, **28**(16), 1705970.
- L. H. Zeng, Q. M. Chen and Z. X. Zhang, *et al.*, Multilayered PdSe<sub>2</sub>/perovskite Schottky junction for fast, self-powered, polarization-sensitive, broadband photodetectors, and image sensor application, *Adv. Sci.*, 2019, **6**(19), 1901134.
- L. Zeng, W. Han and S. E. Wu, *et al.*, Graphene/PtSe<sub>2</sub>/pyramid Si van der Waals Schottky junction for room-temperature broadband infrared light detection, *IEEE Trans. Electron Devices*, 2022, **69**(11), 6212–6216.
- D. Wu, C. Guo and L. Zeng, *et al.*, Phase-controlled van der Waals growth of wafer-scale 2D MoTe<sub>2</sub> layers for integrated high-sensitivity broadband infrared photodetection, *Light: Sci. Appl.*, 2023, **12**(1), 5.
- D. Wu, M. Xu and L. Zeng, *et al.*, In situ fabrication of PdSe<sub>2</sub>/GaN Schottky junction for polarization-sensitive ultraviolet photodetection with high dichroic ratio, *ACS Nano*, 2022, **16**(4), 5545–5555.
- D. Li, R. Qi and P. Zhu, *et al.*, Controllable carrier transfer modulation of ambipolar van der Waals semiconductors toward forksheet FETs, *Appl. Phys. Lett.*, 2024, **124**(21), 213501.
- S. Hu, W. Xiang and B. Liu, *et al.*, Exciton control enables high-performance colloidal quantum well light-emitting diodes, *Appl. Phys. Rev.*, 2024, **11**(2), 021428.
- C. Lan, C. Li and J. C. Ho, *et al.*, 2D WS<sub>2</sub>: from vapor phase synthesis to device applications, *Adv. Electron. Mater.*, 2021, **7**(7), 2000688.
- Y. H. Zhou, Z. B. Zhang and P. Xu, *et al.*, UV-visible photodetector based on I-type heterostructure of ZnO-QDs/monolayer MoS<sub>2</sub>, *Nanoscale Res. Lett.*, 2019, **14**, 364.
- S. Tiwari, S. Veeralingam and S. Badhulika, ZnSe nanoflakes/ZnO quantum dots heterojunction-based bandgap engineered, flexible broadband photodetector on paper substrate, *Mater. Res. Bull.*, 2023, **166**, 112374.

- 19 M. Vemula, S. Veeralingam and S. Badhulika, Hybrid 2D/0D SnSe<sub>2</sub>-SnO<sub>2</sub> vertical junction based high performance broadband photodetector, *J. Alloys Compd.*, 2021, **883**, 160826.
- 20 S. Mukherjee, S. Jana and T. K. Sinha, *et al.*, Infrared tunable, two colour-band photodetectors on flexible platforms using 0D/2D PbS-MoS<sub>2</sub> hybrids, *Nanoscale Adv.*, 2019, **1**(8), 3279–3287.
- 21 P. Zeng, W. Wang and D. Han, *et al.*, MoS<sub>2</sub>/WSe<sub>2</sub> vdW heterostructures decorated with PbS quantum dots for the development of high-performance photovoltaic and broadband photodiodes, *ACS Nano*, 2022, **16**(6), 9329–9338.
- 22 F. He, B. Zhu and B. Cheng, *et al.*, 2D/2D/0D TiO<sub>2</sub>/C<sub>3</sub>N<sub>4</sub>/Ti<sub>3</sub>C<sub>2</sub> MXene composite S-scheme photocatalyst with enhanced CO<sub>2</sub> reduction activity, *Appl. Catal., B*, 2020, **272**, 119006.
- 23 Z. Hu, X. Liu and P. L. Hernández-Martínez, *et al.*, Interfacial charge and energy transfer in van der Waals heterojunctions, *InfoMat*, 2022, **4**, e12290.
- 24 C. Jia, X. Huang and D. Wu, *et al.*, An ultrasensitive self-driven broadband photodetector based on a 2D-WS<sub>2</sub>/GaAs type-II Zener heterojunction, *Nanoscale*, 2020, **12**(7), 4435–4444.
- 25 E. Wu, D. Wu and C. Jia, *et al.*, In-situ fabrication of 2D WS<sub>2</sub>/Si type-II heterojunction for self-powered broadband photodetector with response up to mid-infrared, *ACS Photonics*, 2019, **6**(2), 565–572.
- 26 Y. Xin, X. Wang and Z. Chen, *et al.*, Polarization-sensitive self-powered type-II GeSe/MoS<sub>2</sub> van der Waals heterojunction photodetector, *ACS Appl. Mater. Interfaces*, 2020, **12**(13), 15406–15413.
- 27 J. Duan, P. Chava and M. Ghorbani-Asl, *et al.*, Self-driven broadband photodetectors based on MoSe<sub>2</sub>/FePS<sub>3</sub> van der Waals n-p type-II heterostructures, *ACS Appl. Mater. Interfaces*, 2022, **14**, 11927–11936.
- 28 K. Zhang, T. Zhang and G. Cheng, *et al.*, Interlayer transition and infrared photodetection in atomically thin type-II MoTe<sub>2</sub>/MoS<sub>2</sub> van der Waals heterostructures, *ACS Nano*, 2016, **10**(3), 3852–3858.
- 29 C. Shi, X. Fang and H. B. Zhao, *et al.*, Long-wave infrared emission properties of strain-balanced InAs/In<sub>x</sub>Ga<sub>1-x</sub>As<sub>y</sub>Sb<sub>1-y</sub> type-II superlattice on different substrates, *Rare Met.*, 2024, **43**, 3194–3204.
- 30 A. O. A. Tanoh, N. Gauriot and G. Delport, *et al.*, Directed energy transfer from monolayer WS<sub>2</sub> to near-infrared emitting PbS-CdS quantum dots, *ACS Nano*, 2020, **14**(11), 15374–15384.
- 31 L. B. Luo, H. Hu and X. H. Wang, *et al.*, A graphene/GaAs near-infrared photodetector enabled by interfacial passivation with fast response and high sensitivity, *J. Mater. Chem. C*, 2015, **3**, 4723–4728.
- 32 C. Zhao, Z. Liang and M. Su, *et al.*, Self-powered, high-speed and visible-near infrared response of MoO<sub>3-x</sub>/n-Si heterojunction photodetector with enhanced performance by interfacial engineering, *ACS Appl. Mater. Interfaces*, 2015, **7**, 25981–25990.
- 33 D. Wu, J. Guo and C. Wang, *et al.*, Ultrabroadband and high-detectivity photodetector based on WS<sub>2</sub>/Ge heterojunction through defect engineering and interface passivation, *ACS Nano*, 2021, **15**, 10119–10129.
- 34 Y. Liu, X. Wu and W. Guo, *et al.*, Enhanced performance of a n-Si/p-GaTe heterojunction through interfacial passivation and thermal oxidation, *J. Mater. Chem. C*, 2022, **10**, 11747–11754.
- 35 Y. Y. Lai, Y. W. Yeh and A. J. Tzou, *et al.*, Dependence of photoresponsivity and on/off ratio on quantum dot density in quantum dot sensitized MoS<sub>2</sub> photodetector, *Nanomaterials*, 2020, **10**, 1828.
- 36 H. R. Gutiérrez, N. Perea-López and A. L. Elías, *et al.*, Extraordinary room-temperature photoluminescence in triangular WS<sub>2</sub> monolayers, *Nano Lett.*, 2013, **13**(8), 3447–3454.
- 37 A. Berkdemir, H. R. Gutiérrez and A. R. Botello-Méndez, *et al.*, Identification of individual and few layers of WS<sub>2</sub> using Raman Spectroscopy, *Sci. Rep.*, 2013, **3**, 1755.
- 38 K. A. Alim, V. A. Fonoberov and M. Shamsa, *et al.*, Micro-Raman investigation of optical phonons in ZnO nanocrystals, *J. Appl. Phys.*, 2005, **97**, 124313.
- 39 H. Qiao, Z. Huang and X. Ren, *et al.*, Self-powered photodetectors based on 2D materials, *Adv. Opt. Mater.*, 2019, **8**(1), 1900765.
- 40 S. Qin, H. Xu and M. Liu, *et al.*, Enhanced visible to near-infrared photodetectors made from MoS<sub>2</sub>-based mixed-dimensional structures, *Appl. Surf. Sci.*, 2022, **585**, 152594.
- 41 Z. Li, Z. Li and C. Zuo, *et al.*, Application of nanostructured TiO<sub>2</sub> in UV photodetectors: a review, *Adv. Mater.*, 2022, **34**(28), 2109083.
- 42 H. Yang, R. Luo and K. Shi, *et al.*, Pollution-free interface of 2D-MoS<sub>2</sub>/1D-CuO vdWs heterojunction for high-performance photodetector, *Nanotechnology*, 2024, **35**(10), 105202.
- 43 Y. Yu, Y. Zhang and X. Song, *et al.*, PbS-decorated WS<sub>2</sub> phototransistors with fast response, *ACS Photonics*, 2017, **4**, 950–956.
- 44 X. Wang, D. Yan and C. Zhu, *et al.*, Ultrasensitive photodetector based on 2D WS<sub>2</sub>/AgInGaS quantum dots heterojunction with interfacial charge transfer, *2D Mater.*, 2023, **10**, 045020.
- 45 M. Li, J. S. Chen and P. K. Routh, *et al.*, Distinct optoelectronic signatures for charge transfer and energy transfer in quantum dot-MoS<sub>2</sub> hybrid photodetectors revealed by photocurrent imaging microscopy, *Adv. Funct. Mater.*, 2018, **28**(29), 1707558.
- 46 S. Qin, K. Li and J. Zhu, *et al.*, A new strategy to improve the performance of MoS<sub>2</sub>-based 2D photodetector by synergism of colloidal CuInS<sub>2</sub> quantum dots and surface plasma resonance of noble metal nanoparticles, *J. Alloys Compd.*, 2021, **856**, 158179.
- 47 B. Moon, J. H. Ahn and M. H. Jeong, *et al.*, High-performance and stability of CsPbBr<sub>3</sub>/WSe<sub>2</sub> hybrid photodetectors functionalized using quaternary ammonium ligands, *Adv. Opt. Mater.*, 2023, **11**, 2300414.
- 48 C. S. R. Kolli, V. Selamneni and B. A. M. Martinez, *et al.*, Broadband, ultra-high-responsive monolayer MoS<sub>2</sub>/SnS<sub>2</sub> quantum-dot-based mixed-dimensional photodetector, *ACS Appl. Mater. Interfaces*, 2022, **14**, 15415–15425.

- 49 S. Paul, J. Ghosh and M. T. Hossain, *et al.*, Interfacial charge transfer induced enhanced near-infrared photoluminescence and enhanced visible photodetection in two-dimensional/zero-dimensional Bi<sub>2</sub>Se<sub>3</sub>/CsPbBr<sub>2</sub>I heterojunctions with type-I band alignment, *J. Phys. Chem. C*, 2022, **126**, 16721–16731.
- 50 S. Maity, K. Sarkar and P. Kumar, WO<sub>3</sub>-NP-activated WS<sub>2</sub> layered heterostructures for efficient broadband (254–940 nm) photodetection, *Nanoscale*, 2023, **15**, 16068–16079.
- 51 Q. Feng, Y. Li and F. Gao, *et al.*, Manipulating transfer and separation of photocarriers in monolayer WS<sub>2</sub> via CdSe quantum dot doping, *ACS Photonics*, 2020, **7**(7), 1857–1865.
- 52 S. Zhang, X. Wang and Y. Chen, *et al.*, Ultrasensitive hybrid MoS<sub>2</sub>-ZnCdSe quantum dot photodetectors with high-gain, *ACS Appl. Mater. Interfaces*, 2019, **11**(26), 23667–23672.
- 53 N. Peimyoo, W. Yang and J. Shang, *et al.*, Chemically driven tunable light emission of charged and neutral excitons in monolayer WS<sub>2</sub>, *ACS Nano*, 2014, **8**(11), 11320–11329.
- 54 G. D. Mahan, Excitons in degenerate semiconductors, *Phys. Rev.*, 1967, **153**(3), 882.
- 55 B. A. Gregg, S. G. Chen and R. A. Cormier, Coulomb forces and doping in organic semiconductors, *Chem. Mater.*, 2004, **16**, 4586–4599.
- 56 G. Heliotis, G. Itskos and R. Murray, *et al.*, Hybrid inorganic/organic semiconductor heterostructures with efficient non-radiative energy transfer, *Adv. Mater.*, 2006, **18**(3), 334–338.
- 57 X. Liu, Y. Liu and Y. Ni, *et al.*, Reducing non-radiative recombination energy loss via a fluorescence intensifier for efficient and stable ternary organic solar cells, *Mater. Horiz.*, 2021, **8**(8), 2335–2342.
- 58 K. Shi, J. Li and Y. Xiao, *et al.*, High-response, ultrafast-speed, and self-powered photodetection achieved in InP@ZnS-MoS<sub>2</sub> phototransistors with interdigitated Pt electrodes, *ACS Appl. Mater. Interf.*, 2020, **12**(28), 31382–31391.
- 59 U. Ilyas, R. S. Rawat and T. L. Tan, *et al.*, Oxygen rich p-type ZnO thin films using wet chemical route with enhanced carrier concentration by temperature-dependent tuning of acceptor defects, *J. Appl. Phys.*, 2011, **110**, 093522.
- 60 D. Chen, Z. Wang and T. Ren, *et al.*, Influence of defects on the photocatalytic activity of ZnO, *J. Phys. Chem. C*, 2014, **118**(28), 15300–15307.
- 61 J. Sahu, S. Kumar and V. S. Vats, *et al.*, Lattice defects and oxygen vacancies formulated ferromagnetic, luminescence, structural properties and band-gap tuning in Nd<sup>3+</sup> substituted ZnO nanoparticles, *J. Lumin.*, 2022, **243**, 118673.
- 62 Q. Li, J. Meng and J. Huang, *et al.*, Plasmon-induced pyro-phototronic effect enhancement in self-powered UV-vis detection with a ZnO/CuO p-n junction device, *Adv. Funct. Mater.*, 2022, **32**, 2108903.
- 63 S. Choi, M. R. Phillips and I. Aharonovich, *et al.*, Photo-physics of point defects in ZnO nanoparticles, *Adv. Opt. Mater.*, 2015, **3**(6), 821–827.